Journal of The Electrochemical Society

Electrodeposition of MoS_2 from Dichloromethane

Journal of The Electrochemical Society, 2020 **167** 106511

Electrodeposition of MoS_2 from Dichloromethane

Shibin Thomas,[1,*] Danielle E. Smith,[1] Victoria K. Greenacre,[1] Yasir J. Noori,[2] Andrew L. Hector,[1] C. H. (Kees) de Groot,[2] Gillian Reid,[1] and Philip N. Bartlett[1,z]

[1]*School of Chemistry, University of Southampton, Southampton, SO17 1BJ, United Kingdom*
[2]*School of Electronics and Computer Science, University of Southampton, Southampton, SO17 1BJ, United Kingdom*

The electrodeposition of MoS_2 from dichloromethane (CH_2Cl_2) using tetrabutylammonium tetrathiomolybdate ($[N^nBu_4]_2[MoS_4]$) as a single source precursor is presented. The electrodeposition of MoS_2 from CH_2Cl_2 requires addition of a proton donor to the electrolyte and trimethylammonium chloride (Me_3NHCl) was used for this purpose. Electrochemical Quartz Crystal Microbalance (EQCM) experiments have been employed for a detailed study of the electrochemical mechanism and to study the role of the proton donor. EQCM reveals cathodic electrodeposition of MoS_2 and anodic deposition of MoS_3 as well as an additional corrosion process where the deposited MoS_3 strips back into solution. The electrodeposited MoS_2 films are amorphous in nature. All the films were found to be homogeneous in composition across the electrode area and to be reproducible between experiments. Annealing of the as-deposited films under a sulfur atmosphere results in crystalline MoS_2 as confirmed by energy dispersive X-ray spectroscopy (EDX), Raman spectroscopy and X-ray diffraction. The deposited films were smooth and planar, as observed with scanning electron microscopy (SEM), indicating a layer-by-layer growth typical of transition metal dichalogenides.
 [DOI: 10.1149/1945-7111/ab9c88]

Manuscript submitted May 1, 2020; revised manuscript received June 8, 2020. Published June 23, 2020. *This paper is part of the JES Focus Issue on 2D Layered Materials: From Fundamental Science to Applications. This was Paper 891 presented at the Atlanta, Georgia, Meeting of the Society, October 13–17, 2019.*

Supplementary material for this article is available online

Recently, the layered transition metal dichalcogenides (TMDCs) have attracted considerable attention for technological applications and as an area of scientific curiosity. MoS_2 is particularly important because of its unique electronic[1,2] and optical[3,4] properties, including size dependent band-gaps.[5,6] MoS_2 has a wide range of applications in fields such as energy storage,[7,8] solar cells,[9] electronics,[6] opto-electronics[3] and catalysis.[10,11] It has a layered structure, analogous to graphite, where the S and Mo atoms are bonded covalently to form a 2-dimensional layer and the adjacent layers interact via weak Van der Waals forces.[12] This layered structure allows for the production of single layer or few-layer structures of MoS_2, which possess unique and excellent electronic and optical properties that are different from the bulk phase.

There are a number of existing techniques such as physical or chemical vapour deposition,[13–17] mechanical exfoliation,[6] chemical exfoliation,[18,19] pulsed laser deposition,[20,21] etc., for the deposition of bulk and monolayer MoS_2. However, most of these techniques are expensive, require harsh deposition conditions and some involve the use of potentially toxic reagents. Additionally, scaling up these processes to produce large uniform films is challenging. Therefore, establishing a simple and low cost method for the deposition of MoS_2 is of great importance. Electrodeposition has a number of key advantages as a deposition method, including lower cost and easy scalability. Electrodeposition is essentially a "bottom-up" deposition method where conformal deposition occurs via atom-by-atom growth over the electrode surface. It is typically a low temperature technique, mostly performed in mild conditions with very efficient use of materials (precursors). The deposition occurs only in the areas defined by electrical contact and therefore is well suited for depositing inside complex structures or for producing micro or nano-scale features in advanced devices.

There are several reports in the literature about the electrodeposition of MoS_2 from aqueous electrolytes by employing $[MoS_4]^{2-}$ ions as the precursor.[22–25] However, the use of aqueous electrolytes is limited because of their narrow electrochemical window and the potential hydrolysis of the precursors or oxidation or hydrolysis of the deposited materials. Additionally, hydrogen evolution from the electrode surface is problematic as it can influence the film properties. The use of non-aqueous electrolytes has been proposed to overcome these limitations, however reports are very limited for MoS_2 electrodeposition. There have been attempts to electrodeposit MoS_x ($x = 2–3$) from ethylene glycol[22,23] and ionic liquids[24] using $[MoS_4]^{2-}$ precursors. Murugesan et al. reported the successful electrodeposition of MoS_2 from an ionic liquid, using separate precursors for the Mo and S.[25]

In this paper, we investigate the electrodeposition of MoS_2 from dichloromethane (CH_2Cl_2) using $[N^nBu_4]_2[MoS_4]$ as a single source precursor. CH_2Cl_2 is an excellent solvent for electrodeposition as it is relatively inert and is either non-coordinating or only weakly coordinating.[26] We have recently reported the electrodeposition of technologically important materials such as Bi_2Te_3,[27] GeSbTe[28–30] and HgTe[31] by using CH_2Cl_2 as the electrolyte solvent. In this paper, the electrochemical mechanism of MoS_2 deposition and the role of an external proton donor, revealed with the help of EQCM, are investigated and discussed in detail. Microscopic and spectroscopic characterisation of the deposits are also presented.

Experimental

Electrochemistry.—All the electrolyte preparations, electrochemical characterisations and electrodeposition were performed inside an N_2 filled recirculating glove box (Belle Technology, UK) with sub-10 ppm O_2 and H_2O levels. Electrolyte solutions were prepared in anhydrous CH_2Cl_2 (Sigma-Aldrich, 95%), dried and degassed by refluxing with CaH_2 followed by distillation. The water content in dried CH_2Cl_2 was ca. 18 ppm determined by Karl Fischer titration. 0.1 M $[N^nBu_4]Cl$ (Sigma-Aldrich, ⩾99.0%, as-received) was used as the supporting electrolyte. Trimethylammonium chloride (Sigma-Aldrich) served as the proton donor.

All cyclic voltammetry and electrodeposition experiments were carried out in a three-electrode system using an Autolab potentiostat (μAUT70706). A Pt mesh was used as the counter electrode and the reference electrode was Ag/AgCl (0.1 M $[N^nBu_4]Cl$ in CH_2Cl_2). The Pt mesh counter electrode was cleaned by rinsing with de-ionised water and heating in a butane/propane mix flame (70% butane, 30% propane). A 0.4 cm diameter titanium nitride (TiN) or Pt substrate was employed as the working electrode. The EQCM (QCM 200, SRS) system used 5 MHz AT-cut quartz crystal (1.3 cm diameter) with Pt

*Electrochemical Society Member.
[z]E-mail: P.N.Bartlett@soton.ac.uk

coatings. TiN was chosen as an electrode material because it is a technologically relevant electrode material for micro- and nano-device fabrication. After the electrodeposition, the substrates were cleaned with fresh CH_2Cl_2 solvent followed by rinsing with isopropyl alcohol and dried prior to characterisation. The samples were annealed in a tube furnace under an N_2 atmosphere by applying 100 °C for 10 min followed by 500 °C for 2 h in the presence of sulfur.

Film characterisation.—A scanning electron microscope (SEM, Philips XL30 ESEM) was used to image the deposits after electrodeposition. The elemental composition was obtained by energy dispersive X-ray spectroscopy (EDX) coupled to SEM, using a Thermo Scientific NORAN System 7 X-ray Microanalysis System. Wavelength dispersive X-ray spectroscopy (WDX) was employed for obtaining elemental composition with higher spectral resolution. The calibration of the EDX/WDX quantification was confirmed by comparison to a standard MoS_2 single crystal sample prepared by chemical vapour transport (CVT, Ossila Technologies). Raman spectra were obtained using Renishaw Inc. spectrometer with 532 nm laser excitation. X-Ray diffraction (XRD) patterns were collected in grazing incidence mode ($\theta_1 = 1°$) using a Rigaku SmartLab diffractometer (Cu-K_α, $\lambda = 1.5418$ Å) with parallel X-ray beam and a Hypix detector used in 1D mode.

Results and Discussion

$[NH_4]_2[MoS_4]$ has been widely employed as a precursor for aqueous electrodeposition of MoS_2.[32,33] However, it is not sufficiently soluble in CH_2Cl_2 for non-aqueous electrodeposition. Therefore $[N^nBu_4]_2[MoS_4]$ was synthesised and used as a single source precursor to deliver both the Mo and S. $[N^nBu_4]_2[MoS_4]$ offers excellent solubility in CH_2Cl_2 and contains the same cation as the supporting electrolyte ($[N^nBu_4]Cl$).

The electrochemical behaviour of $[N^nBu_4]_2[MoS_4]$ in CH_2Cl_2 was investigated by conducting cyclic voltammetry (CV) experiments. The black curve in Fig. 1a shows the background CV of the supporting electrolyte (0.1 M $[N^nBu_4]Cl$) in CH_2Cl_2 recorded on a Pt working electrode. The CV shows a wide cathodic solvent window (~2.7 V). The red curve in Fig. 1a shows the CV of a 5 mM solution of $[N^nBu_4]_2[MoS_4]$ in CH_2Cl_2 with 0.1 M $[N^nBu_4]Cl$ supporting electrolyte. The addition of $[N^nBu_4]_2[MoS_4]$ induces only minor changes to the CV. A small increase in the reduction current starting from −1.15 V results in a small peak at −1.3 V being observed. Further exponential increase in current after −1.6 V is due to the cathodic breakdown of the solvent/electrolyte. On the anodic scan, a small broad peak is observed at around +0.9 V. The current density in the cathodic regime is too small to result in any deposition of the target material. However, we tried to polarise the working electrode at a potential beyond the observed peak potential (−1.3 V), but this neither produced any colour change on the electrode nor the presence of any micro-scale deposit.

These results show that MoS_2 cannot be electrodeposited from $[N^nBu_4]_2[MoS_4]$ on its own in CH_2Cl_2. This is consistent with reports in the literature, where the reduction of $[MoS_4]^{2-}$ ions to MoS_2 requires the presence of protons in the electrolyte to remove the excess sulfur.[23] For example, in the case of aqueous electrodeposition of MoS_2 using $[NH_4]_2[MoS_4]$, the deposition occurs *via* the following the reaction:[34]

$$MoS_4^{2-} + 2\,e^- + 4H^+ \rightarrow MoS_2 + 2H_2S \qquad [1]$$

To overcome this problem, Me_3NHCl was added to the electrolyte as the proton donor since it is soluble in CH_2Cl_2, does not react with the $[MoS_4]^{2-}$ anion, and is able to release H^+ ions into the solution. The addition of Me_3NHCl causes significant changes to the CV of $[N^nBu_4]_2[MoS_4]$ in CH_2Cl_2, especially in the cathodic potential range. The red curve in Fig. 1b shows the CV from an electrolyte containing 5 mM $[N^nBu_4]_2[MoS_4]$, 0.2 M Me_3NHCl with 0.1 M $[N^nBu_4]Cl$ in CH_2Cl_2. In the cathodic scan, a large reduction current starting from −0.35 V is observed, which continues to increase until −1.85 V, where the potential is reversed for the anodic sweep. Despite the large reduction current, no clear reduction peaks were identified in the CV. It is important to note that the proton donor is not electrochemically inert, as evidenced from the CV of the background electrolyte (black curve in Fig. 1b). This means that the large reduction current observed in the CV of $[N^nBu_4]_2[MoS_4]$ with Me_3NHCl must include a significant contribution from the cathodic decomposition of the proton donor, which is difficult to resolve from the current response due to the $[MoS_4]^{2-}$ reduction. In comparison with the CV of the background electrolyte (black curve in Fig. 1b), the addition of $[N^nBu_4]_2[MoS_4]$ to the electrolyte results in a reduction of cathodic current in the CV (red curve in Fig. 1b), presumably due to the modification of the electrode surface by the deposition of MoS_x.

On the anodic scan, there is an oxidation peak around +0.8 V similar to that observed in the CV without the proton donor (red curve in Fig. 1a). This corresponds to the oxidation of $[MoS_4]^{2-}$ ions

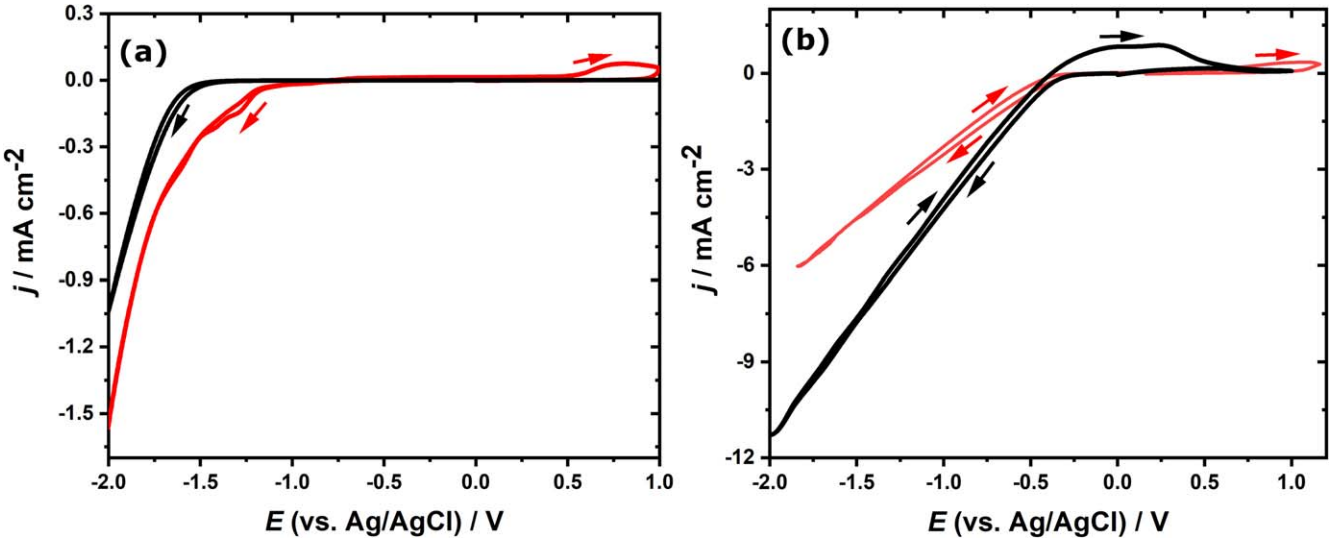

Figure 1. (a) Cyclic voltammogram of 5 mM $[N^nBu_4]_2[MoS_4]$ in CH_2Cl_2 on a Pt electrode. The black line shows the background CV for CH_2Cl_2. (b) Cyclic voltammogram of 5 mM $[N^nBu_4]_2[MoS_4]$ and 0.2 M Me_3NHCl in CH_2Cl_2 on a Pt electrode. The black line shows the background CV for 0.2 M Me_3NHCl in CH_2Cl_2 electrolyte. In each case, the supporting electrolyte is 0.1 M $[N^nBu_4]Cl$ and the scan rate is 50 mV s^{-1}. Arrows indicate the direction of potential scanning, the starting potential is 0.0 V.

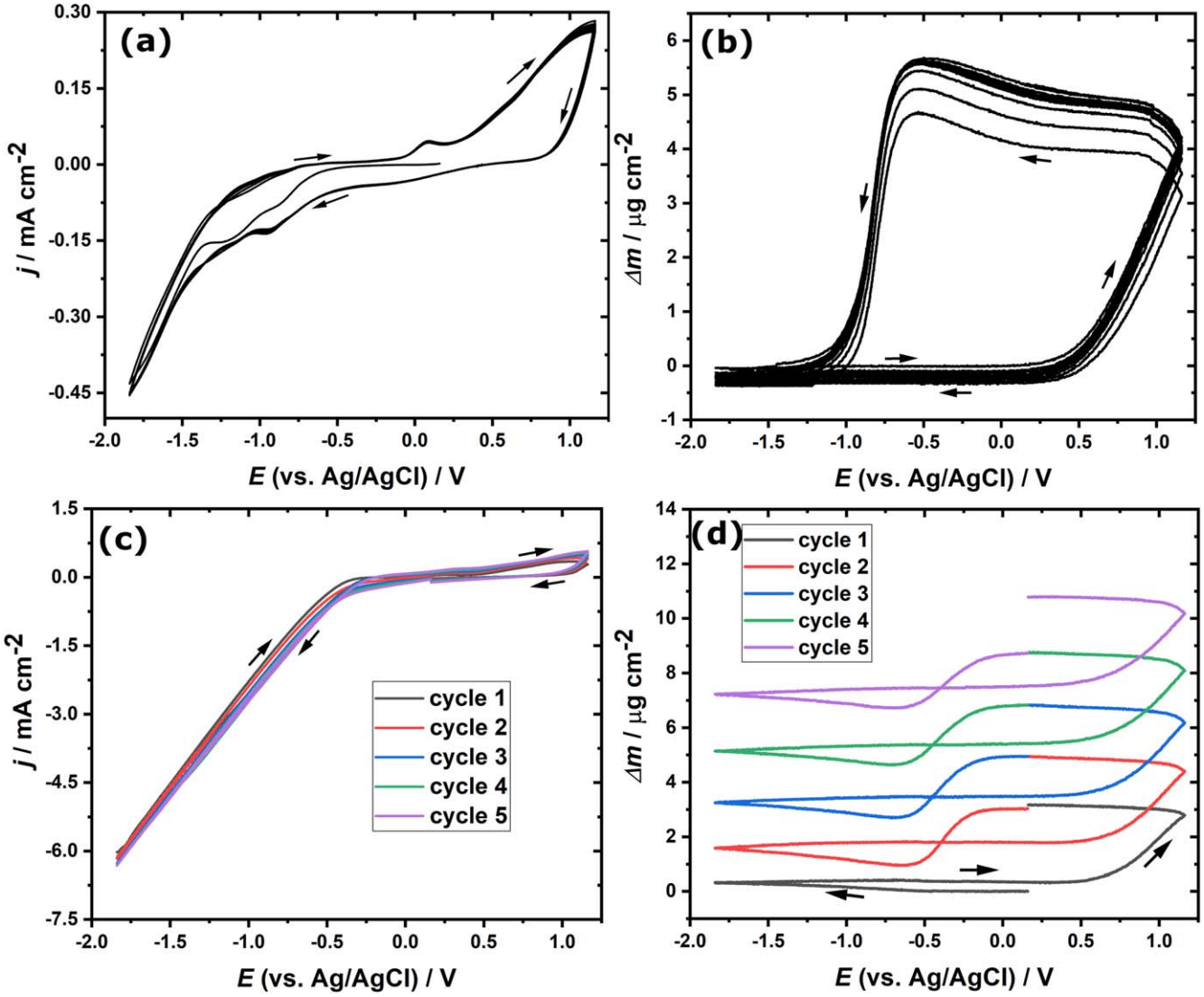

Figure 2. (a) Multicycle CVs of 5 mM $[N^nBu_4]_2[MoS_4]$ in CH_2Cl_2 on a Pt electrode. (b) The change of mass during the CVs of 5 mM $[N^nBu_4]_2[MoS_4]$ in CH_2Cl_2 without H^+ donor. (c) Multicycle CVs of 5 mM $[N^nBu_4]_2[MoS_4]$ with 0.2 M Me_3NHCl in CH_2Cl_2 on a Pt electrode. (d) The change of mass during the CVs of 5 mM $[N^nBu_4]_2[MoS_4]$ with 0.2 M Me_3NHCl as H^+ donor. In each case, the supporting electrolyte is 0.1 M $[N^nBu_4]Cl$ and the scan rate is 50 mV s^{-1}. Arrows indicate the direction of potential scanning, the starting point is 0.0 V.

to deposit MoS_3 following the reaction:[34,35]

$$MoS_4^{2-} \rightarrow MoS_3 + \frac{1}{8}S_8 + 2e^- \quad [2]$$

Note that the proton donor is not necessary for the anodic deposition of MoS_3, which is the reason this peak at +0.8 V is observed in both the CVs regardless of the presence of proton donor.

In order to determine whether the addition of the proton donor facilitates the cathodic deposition of MoS_2, potentiostatic electrodeposition was carried out from CH_2Cl_2 electrolyte containing 5 mM $[N^nBu_4]_2[MoS_4]$, 0.2 M Me_3NHCl and 0.1 M $[N^nBu_4]Cl$ by polarizing the electrode at −1.5 V for 30 min. A yellowish- brown coloured thin film was obtained on the working electrode, which confirms the possibility of cathodic electrodeposition to yield MoS_x thin films. Prior to detailed characterisation of the films, it is important to gain deeper insights on the electrochemistry, especially because the addition of a proton donor makes the voltammograms complicated due to its early decomposition. A thorough understanding of the different electrochemical processes occurring at the interface during a CV experiment is important in choosing the applied potential for deposition and for controlling the growth rate and purity of the deposits. The inclusion of decomposition products from the proton donor, especially at large negative potentials, might introduce impurities in the thin films.

EQCM is a powerful tool used in electrochemical measurements to follow micro-gravimetric changes occurring at the electrode. In order to gain deeper insights on the voltammograms, EQCM was used to follow the changes on cycling the potential and the associated mass changes were estimated using the Sauerbrey equation.[36]

$$\Delta f = -\frac{2f_0^2 \Delta m}{A\sqrt{\rho_q \mu_q}} \quad [3]$$

Where Δf is the frequency change, f_0 is the resonance frequency of the crystal (≈5 MHz), Δm is the mass change, A is the surface area of the electrode (1.33 cm^2), ρ_q is the density of quartz (2.65 g cm^{-3}) and μ_q is the shear modulus of the quartz (2.95×10^{11} g cm^{-1} s^{-2}).

To study the role of the proton donor in electrodeposition, EQCM measurements were performed in electrolytes with and without Me_3NHCl in the solution. Figure 2a shows the multicycle CVs of 5 mM $[N^nBu_4]_2[MoS_4]$ in CH_2Cl_2 without proton donor and Fig. 2b

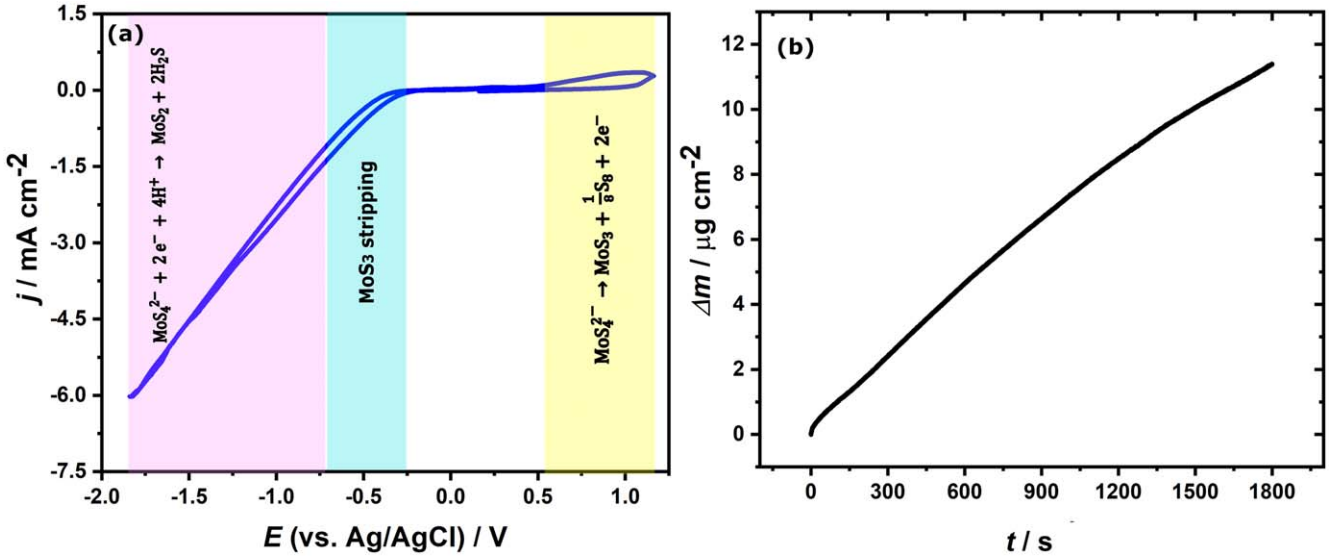

Figure 3. (a) Schematic representation of various electrochemical reactions occurring during a CV of $[N^nBu_4]_2[MoS_4]$ with Me_3NHCl as H^+ donor in CH_2Cl_2. (b) The change of mass during the potentiostatic deposition at −1.0 V from CH_2Cl_2 containing 5 mM $[N^nBu_4]_2[MoS_4]$ and 0.2 M Me_3NHCl. The supporting electrolyte is 0.1 M $[N^nBu_4]Cl$.

shows the corresponding mass change during the CVs. No mass change is observed when the CV is scanned cathodic from 0.0 to −1.85 V, indicating the absence of any deposition in the cathodic potential window when $[N^nBu_4]_2[MoS_4]$ alone is used. In contrast, a rapid and steady increase in mass is observed on the anodic scan corresponding to the oxidation peak around +0.9 V. This mass change is due to the anodic deposition of MoS_3 according to equation 2. This deposition mechanism does not require protons and hence occurs in the electrolyte containing just $[N^nBu_4]_2[MoS_4]$. The mass deposited in the first anodic scan is 3.1 μg cm^{-2} which corresponds to a charge of 6 mC cm^{-2}, and a small gradual increase in mass is observed until −0.55 V on the reverse scan. From the second cycle of the CV onwards, an interesting stripping reaction is observed starting from −0.55 V, where all the mass gained during the anodic oxidation is lost when the potential approaches −0.98 V. This is attributed to the corrosion of electrodeposited MoS_3 stripping back to solution as some soluble species. This process of anodic deposition and subsequent corrosion in cathodic scan is repeated in each CV scan recorded, and the resultant mass gain on the electrode is zero.

Note that the stripping charge for MoS_3 is about half that of the deposition charge, which is indicative of side reactions at anodic potentials. The excess charge passed during anodic deposition presumably corresponds to Cl_2 evolution, as both the supporting electrolyte ($[N^nBu_4]Cl$) and the proton donor (Me_3NHCl) provide free Cl^- ions in solution.

Figure 2c shows the multicycle CVs of 5 mM $[N^nBu_4]_2[MoS_4]$ with 0.2 M Me_3NHCl in CH_2Cl_2 and Fig. 2d shows the corresponding mass changes during each cycle. In contrast to the CVs without proton donor (Fig. 2a), cathodic deposition is possible when Me_3NHCl is added to the electrolyte, as evidenced by the increase of mass in the E vs Δm plot. A small increase in mass is observed from −0.6 V until −1.85 V in the cathodic scan, which presumably corresponds to the reduction of $[MoS_4]^{2-}$ to MoS_2 as shown in equation 1. This information regarding the onset and the range of cathodic reduction potentials revealed by the EQCM is highly important, as the current response in the CVs is very complicated and otherwise difficult to analyse due to the decomposition of the proton donor. The EQCM shows that material can be electrodeposited by applying potentials more negative than −0.6 V. Knowledge of this onset of reduction potential is useful in controlling the growth rate as well as the purity and composition of the deposit, as decomposition products from the solvent, electrolyte or proton donor formed at more negative potentials could contaminate any deposit.

The mass increment in the cathodic scan from each cycle is approximately 0.6 μg cm^{-2}. The mass remains nearly constant on the reverse scan until +0.48 V. The electrochemical behaviour of the electrolyte in the anodic potential range is quite similar to the behaviour observed in CVs without proton donor. In the CV, a gradual increase in current, characterised by a broad oxidation peak around +0.9 V, is observed between +0.48 V and +1.15 V. A relatively large increase in mass is observed in this potential window, which corresponds to the deposition of MoS_3. Approximately 3.1 μg cm^{-2} of mass is deposited in a single scan in the anodic range. It is interesting to note that the mass increase by anodic deposition in a single cycle is about 5 times that of the mass deposited by the cathodic deposition. A similar corrosion process to that observed in CVs without proton donor is evident here as well. From the second cycle of the CV onwards, the E vs Δm plots shows cathodic stripping of the deposits starting from −0.11 V and continuing until −0.6 V. This removes about 70%–75% of the MoS_x deposits on each cycle. However, a steady increase in mass with consecutive CV cycles is clearly observable in Fig. 2d, which demonstrates the importance of a proton donor in obtaining MoS_2 by cathodic electrodeposition.

A schematic depicting all the suggested electrochemical reactions during different stages of the CV is shown in Fig. 3a. In order to confirm the cathodic deposition of MoS_2, potentiostatic deposition has been performed in EQCM by polarising the working electrode at −1.0 V for 30 min. Figure 3b shows the plot of time vs mass during the potentiostatic deposition. The graph shows a linear increase of mass with time and the growth rate is 6.7 ng cm^{-2} s^{-1}. At the end of 30 min deposition, the mass of the deposit obtained is 11.5 μg cm^{-2}. By plotting the charge vs mass curve from EQCM, it is possible to calculate the apparent molar mass of the material being deposited during the CV or potentiostatic deposition.

$$M = \frac{mFZ}{Q} \quad [4]$$

Where M is the molar mass, Z is the number of electrons transferred, m is the mass of material deposited, F is the Faraday constant and Q is the charge passed. Considering a complete two-electron reduction process and assuming 100% faradaic efficiency, the theoretical apparent molar mass for MoS_2 is 80.03 g mol^{-1}. However, the

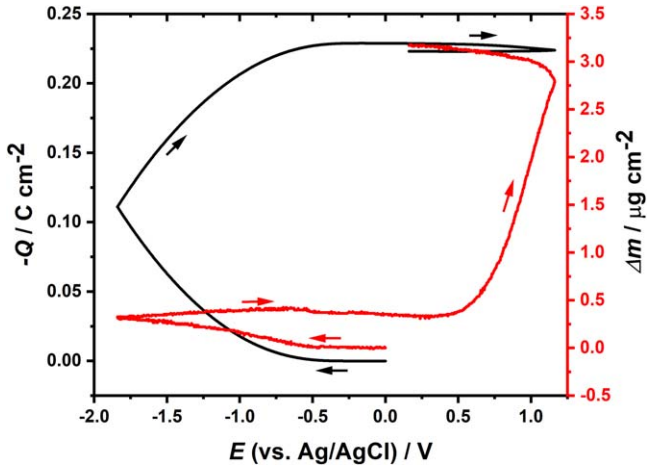

Figure 4. The evolution of charge (black line) and mass (red line) with potential during 1st cycle of the CV recorded in CH_2Cl_2 containing 5 mM $[N^nBu_4]_2[MoS_4]$ and 0.2 M Me_3NHCl. The supporting electrolyte is 0.1 M $[N^nBu_4]Cl$ and the scan rate is 50 mV s^{-1}. Arrows indicate the direction of potential scanning, the starting point is 0.0 V.

calculated apparent molar mass values for the cathodic deposition of MoS_2 is found to be very much smaller than the theoretical value, indicating a very low current efficiency (<10%) between −0.6 and −1.85 V. This confirms the fact that the majority of the charge passed during cathodic scan has been used for the decomposition of the electrolyte, primarily for the Me_3NHCl breakdown. On the other hand, the current efficiency values are found to be much higher in the potential range from +0.5 to +1.15 V where MoS_3 is being deposited. The experimental M/z value is 67 g mol^{-1} while the theoretical M/z value is 96.06 g mol^{-1}, resulting in current efficiency of about 70%, and the deviation (from 100%) is accounted for by the occurrence of side reactions such as Cl_2 evolution. This observation is supported by the plot of the reduction charge ($-Q$) and mass change (Δm) as a function of applied potential, as shown in Fig. 4. A relatively large quantity of charge is passed between −0.6 to −1.85 V in the cathodic range, both in the forward and backward scan. However, the corresponding mass change is quite small (~0.5 μg cm^{-2}). On the anodic scan from +0.5 V to +1.15 V, the E vs $-Q$ curve shows a small linear decrease in $-Q$ corresponding to an oxidation charge but this is associated with a significant linear increase in mass from MoS_3 deposition (around 2.5 μg cm^{-2}). The total charge passed in the anodic potential range is two orders of magnitude smaller than that passed in the cathodic range, however, the mass gain is 5 times higher than that obtained during cathodic scan.

In order to enable further characterisation of the deposited material, potentiostatic electrodeposition was carried out onto a TiN substrate by applying −0.8 V for 1 h. The applied potential, −0.8 V, was chosen based on the EQCM results, where minimal effects of electrolyte decomposition are expected. A 60 min deposition was carried out to obtain sufficiently thick deposits to allow reliable characterisation. The as-deposited thin film was shown to be amorphous by X-ray diffraction. This is not unexpected as the deposition was carried out at room temperature, and other work in the literature reported formation of poorly crystalline MoS_2 at ambient conditions.[23,37,38] In order to crystallise the film, annealing treatment was performed in a tube furnace by applying 100 °C for 10 min followed by 500 °C for 2 h under N_2 in the presence of sulfur. After annealing, the colour of the film had changed from yellowish-brown to a reflective metallic appearance, typical of MoS_2. A broad peak centred on 14.4° (2θ) is observed in the X-ray diffraction pattern (Fig. S3 ESI is available online at stacks.iop.org/JES/167/106511/mmedia) corresponding to the (002) plane of 2H-MoS_2, suggesting a preferential orientation perpendicular to the crystallographic planes.

Figure 5a depicts a top-view SEM image of the annealed deposit. The image shows a very flat, smooth and mostly continuous layered deposit homogeneously covering the electrode, with a few cracks on the surface. The occurrence of cracks is likely to be due to the internal stresses during the growth or annealing, especially when long-time depositions are used to produce thicker films. No particulates are identified on the surface of the deposit, and the flat surface indicates a laminar structure typical of MoS_2. Figure 5b shows the energy dispersive X-ray (EDX) spectrum recorded from the deposit. The spectrum shows a strong signal at 2.3 keV, which indicates the presence of Mo and/or S. The Si and Ti signals are from the electrode substrate used. Note that the Mo-L_α (2.29 keV) and S-K_α (2.30 keV) peaks appear overlapped in the EDX spectrum due to the low spectral resolution and inability to differentiate the Mo (L_α) and S (K_α) features. We therefore used wavelength dispersive X-ray (WDX) spectroscopy, which provides a better spectral resolution. The inset of Fig. 5b displays the WDX spectrum, and clearly shows two distinct peaks, one at 2.29 keV due to Mo-L_α and the second one at 2.30 due to S-K_α. The S/Mo ratio determined by WDX quantification is between 1.9 and 2.1. A commercial single crystal MoS_2 sample was used as a calibration standard. The

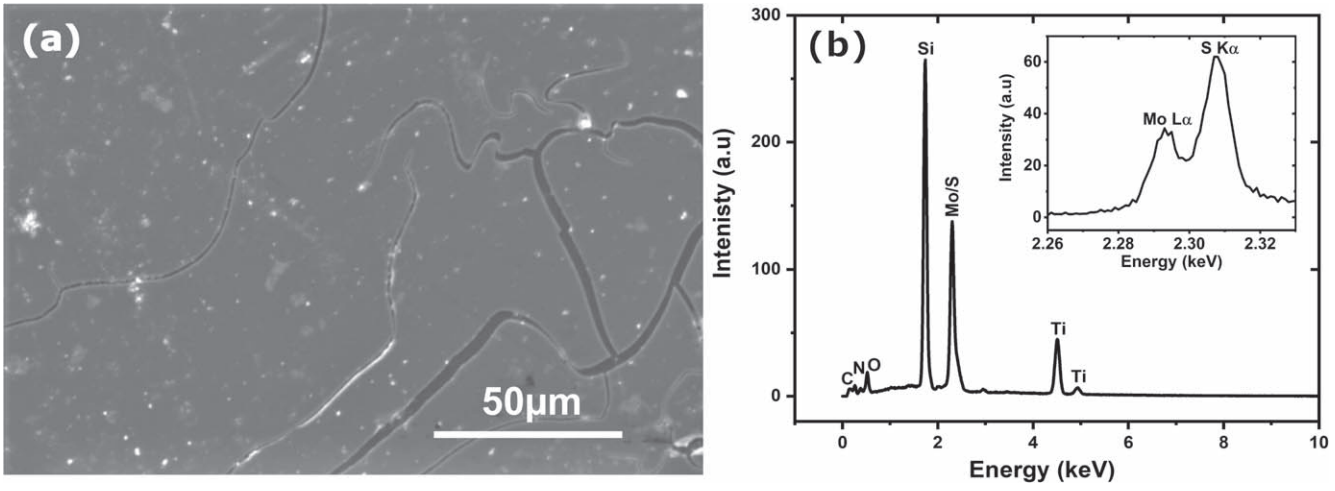

Figure 5. (a) Top-view SEM image of the annealed deposit obtained after potentiostatic deposition at −0.8 V for 60 min from CH_2Cl_2 containing 5 mM $[N^nBu_4]_2[MoS_4]$ and 0.2 M Me_3NHCl with 0.1 M $[N^nBu_4]Cl$ supporting electrolyte. (b) EDX profile of the deposited film after annealing. The inset shows WDX spectrum for Mo-L_α and S-K_α lines.

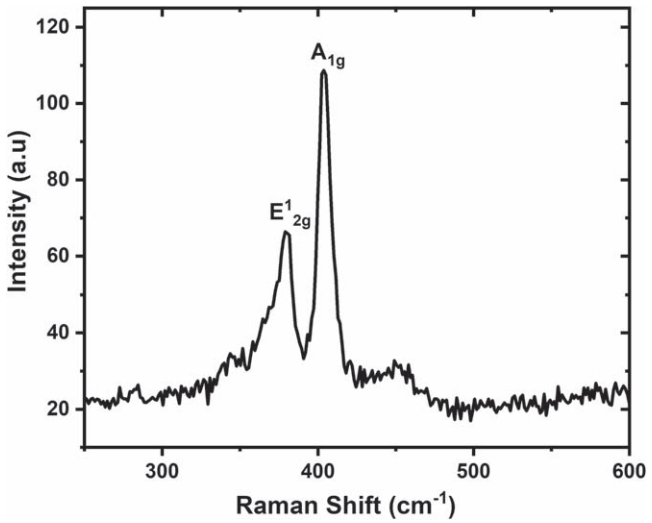

Figure 6. Raman spectrum recorded from annealed MoS_2 deposit using 532 nm laser excitation.

as-deposited film was slightly sulfur-rich, having S/Mo ratio between 2.4 to 2.7 (Fig. S4 ESI). The excess sulfur in the film might be due to the inclusion of elemental sulfur and/or S_2^{2-} produced in solution from the electrochemical reaction at the anode (See equation 2). It appears that annealing of the film results in the removal of the excess sulfur by evaporation, inducing an increase in density and compactness of the film due to restructuring (amorphous to crystalline) at the elevated temperature.

The applied potential is found to be a critical parameter determining the purity of the deposits, as the films obtained at more negative potentials contained significant impurities, such as C and Cl due to the decomposition of the electrolyte (Fig. S5 ESI). The deposits obtained by applying −0.8 and −1.0 V were found to be relatively pure. Therefore, electrodeposition by applying potentials more positive than −1.0 V is recommended for obtaining good quality films.

The Raman spectrum recorded from the annealed deposit using 532 nm laser excitation is shown in Fig. 6. The spectrum shows two prominent peaks, which are the E_{2g} (379.5 cm^{-1}) and the A_{1g} (403.7 cm^{-1}) modes for 2H-MoS_2. The E_{2g} mode is an in-plane vibrational and the A_{1g} mode is the out-of-plane vibration mode of S atoms in the vertical direction.[4] The small broad peak at 454 cm^{-1} corresponds to the 2LA(M) vibration mode of MoS_2. The frequency difference between the E_{2g} and A_{1g} peaks, which is indicative of the number of layers, is 24.2 cm^{-1}, corresponding to a multilayer MoS_2 film.[39]

Conclusions

Electrodeposition of MoS_2 in dichloromethane using $[N^nBu_4]_2[MoS_4]$ as a single source precursor has been successfully demonstrated. Addition of an external proton donor is found to be essential for the non-aqueous electrodeposition of MoS_2 using the tetrathiomolybdate ion. A detailed investigation on the role of Me_3NHCl as proton donor and the electrochemical mechanism was conducted using electrochemical quartz crystal microbalance experiments, and the deposition conditions were optimised. The as-deposited thin films are amorphous in nature, but upon annealing give crystalline MoS_2. The electrodeposition technique allows deposition of films with good homogeneity over the electrode, as well as good reproducibility in their composition. The compositional and structural quality of the MoS_2 deposits were confirmed by SEM, EDX/WDX, X-ray diffraction and Raman spectroscopy. The present study provides a simple and low cost alternative for the deposition of MoS_2. Future work will focus on controlling the electrodeposition parameters aiming to obtain mono- or few layer MoS_2 for device level applications.

Acknowledgments

The authors thank EPSRC for support via EP/P025137/1, EP/N035437/1 and EP/N509747/1, and for funding the Smartlab diffractometer under EP/ K00509X/1 and EP/K009877/1.

ORCID

Shibin Thomas https://orcid.org/0000-0002-7735-788X
Yasir J. Noori https://orcid.org/0000-0001-5285-8779
Andrew L. Hector https://orcid.org/0000-0002-9964-2163
C. H. (Kees) de Groot https://orcid.org/0000-0002-3850-7101
Gillian Reid https://orcid.org/0000-0001-5349-3468
Philip N. Bartlett https://orcid.org/0000-0002-7300-6900

References

1. H. Wang, C. Li, P. Fang, Z. Zhang, and J. Z. Zhang, *Chem. Soc. Rev.*, **47**, 6101 (2018).
2. S. Das, H.-Y. Chen, A. V. Penumatcha, and J. Appenzeller, *Nano Lett.*, **13**, 100 (2012).
3. A. Splendiani, L. Sun, Y. Zhang, T. Li, J. Kim, C.-Y. Chim, G. Galli, and F. Wang, *Nano Lett.*, **10**, 1271 (2010).
4. H. Li, Q. Zhang, C. C. R. Yap, B. K. Tay, T. H. T. Edwin, A. Olivier, and D. Baillargeat, *Adv. Funct. Mater.*, **22**, 1385 (2012).
5. T. Lin, B. Kang, M. Jeon, C. Huffman, J. Jeon, S. Lee, W. Han, J. Lee, S. Lee, and G. Yeom, *ACS Appl. Mater. Interfaces*, **7**, 15892 (2015).
6. B. Radisavljevic, A. Radenovic, J. Brivio, V. Giacometti, and A. Kis, *Nat. Nanotechnol.*, **6**, 147 (2011).
7. E. Cha, M. D. Patel, J. Park, J. Hwang, V. Prasad, K. Cho, and W. Choi, *Nat. Nanotechnol.*, **13**, 337 (2018).
8. A. L. Santhosha, P. K. Nayak, K. Pollok, F. Langenhorst, and P. Adelhelm, "Electrochemical and solid-state letters." *J. Phys. Chem. C*, **123**, 12126 (2019).
9. M.-L. Tsai, S.-H. Su, J.-K. Chang, D.-S. Tsai, C.-H. Chen, C.-I. Wu, L.-J. Li, L.-J. Chen, and J.-H. He, *ACS Nano*, **8**, 8317 (2014).
10. Y. Li, H. Wang, L. Xie, Y. Liang, G. Hong, and H. Dai, *J. Am. Chem. Soc.*, **133**, 7296 (2011).
11. H. I. Karunadasa, E. Montalvo, Y. Sun, M. Majda, J. R. Long, and C. J. Chang, *Science*, **335**, 698 (2012).
12. H. Rydberg, M. Dion, N. Jacobson, E. Schröder, P. Hyldgaard, S. Simak, D. C. Langreth, and B. I. Lundqvist, *Phys. Rev. Lett.*, **91**, 126402 (2003).
13. Y. H. Lee, X. Q. Zhang, W. Zhang, M. T. Chang, C. T. Lin, K. D. Chang, Y. C. Yu, J. T. W. Wang, C. S. Chang, and L. J. Li, *Adv. Mater.*, **24**, 2320 (2012).
14. L. Tao, K. Chen, Z. Chen, W. Chen, X. Gui, H. Chen, X. Li, and J.-B. Xu, *ACS Appl. Mater. Interfaces*, **9**, 12073 (2017).
15. J. Zhang et al., *ACS Nano*, **8**, 6024 (2014).
16. S. Wu, C. Huang, G. Aivazian, J. S. Ross, D. H. Cobden, and X. Xu, *ACS Nano*, **7**, 2768 (2013).
17. Z. P. Ling et al., *Opt. Express*, **23**, 13580 (2015).
18. A. Jawaid, D. Nepal, K. Park, M. Jespersen, A. Qualley, P. Mirau, L. F. Drummy, and R. A. Vaia, *Chem. Mater.*, **28**, 337 (2016).
19. X. Yang, W. Fu, W. Liu, J. Hong, Y. Cai, C. Jin, M. Xu, H. Wang, D. Yang, and H. Chen, *J. Mater. Chem. A*, **2**, 7727 (2014).
20. T. A. Loh and D. H. Chua, *ACS Appl. Mater. Interfaces*, **6**, 15966 (2014).
21. C. R. Serrao, A. M. Diamond, S.-L. Hsu, L. You, S. Gadgil, J. Clarkson, C. Carraro, R. Maboudian, C. Hu, and S. Salahuddin, *Appl. Phys. Lett.*, **106**, 052101 (2015).
22. E. A. Ponomarev, *J. Electrochem. Soc.*, **144**, L277 (1997).
23. A. Albu-Yaron, C. Levy-Clement, and J. Hutchison, *Electrochem. Solid-State Lett.*, **2**, 627 (1999).
24. D. W. Redman, M. J. Rose, and K. J. Stevenson, *Langmuir*, **33**, 9354 (2017).
25. S. Murugesan, A. Akkineni, B. P. Chou, M. S. Glaz, D. A. Vanden Bout, and K. J. Stevenson, *ACS Nano*, **7**, 8199 (2013).
26. K. M. Kadish and J. E. Anderson, *Pure Appl. Chem.*, **59**, 703 (1987).
27. L. Meng, K. Cicvarić, A. L. Hector, C. H. de Groot, and P. N. Bartlett, *J. Electroanal. Chem.*, **839**, 134 (2019).
28. G. P. Kissling, R. Huang, A. Jolleys, S. L. Benjamin, A. L. Hector, G. Reid, W. Levason, C. K. de Groot, and P. N. Bartlett, *J. Electrochem. Soc.*, **165**, D557 (2018).
29. P. N. Bartlett et al., *Mater. Horiz.*, **2**, 420 (2015).
30. R. Huang et al., *Faraday Discuss.*, **213**, 339 (2019).
31. G. P. Kissling, M. Aziz, A. W. Lodge, W. Zhang, M. Alibouri, R. Huang, A. L. Hector, G. Reid, C. H. de Groot, and R. Beanland, *J. Electrochem. Soc.*, **165**, D802 (2018).
32. A. S. Aliyev, M. Elrouby, and S. F. Cafarova, *Mater. Sci. Semicond. Process.*, **32**, 31 (2015).
33. E. A. Ponomarev, M. Neumann-Spallart, G. Hodes, and C. Lévy-Clément, *Thin Solid Films*, **280**, 86 (1996).
34. H. Vrubel and X. Hu, *ACS Catal.*, **3**, 2002 (2013).
35. C. G. Morales-Guio and X. Hu, *Acc. Chem. Res.*, **47**, 2671 (2014).
36. G. Sauerbrey, *Z. Phys.*, **155**, 206 (1959).
37. A. Lamouchi, I. B. Assaker, and R. Chtourou, *J. Mater. Sci.*, **52**, 4635 (2017).
38. R. Chaabani, A. Lamouchi, B. Mari, and R. Chtourou, *Mater. Res. Express*, **6**, 115902 (2019).
39. C. Lee, H. Yan, L. E. Brus, T. F. Heinz, J. Hone, and S. Ryu, *ACS Nano*, **4**, 2695 (2010).
40. A. Albu-Yaron, C. Lévy-Clément, A. Katty, S. Bastide, and R. Tenne, *Thin Solid Films*, **361–362**, 223 (2000).